Chemical Engineering Journal 481 (2024) 148547

Contents lists available at ScienceDirect

Chemical Engineering Journal

journal homepage: www.elsevier.com/locate/cej

Kinetically promoted hydrogen generation by Ru nanoparticles decorated CoB_2O_4 on mesoporous carbon spheres with rich oxygen vacancies for $NaBH_4$ hydrolysis

Huatong Li [a], Xinran Hu [a], Lixia Wang [a], Luyan Shi [a], Tayirjan Taylor Isimjan [b,*], Xiulin Yang [a,*]

[a] Guangxi Key Laboratory of Low Carbon Energy Materials, School of Chemistry and Pharmaceutical Sciences, Guangxi Normal University, Guilin 541004, China
[b] Saudi Arabia Basic Industries Corporation (SABIC) at King Abdullah University of Science and Technology (KAUST), Thuwal 23955-6900, Saudi Arabia

ARTICLE INFO

Keywords:
Ru/CoB_2O_4@C
Oxygen vacancies
Synergistic effect
$NaBH_4$ hydrolysis
DFT calculation

ABSTRACT

Developing heterostructured catalysts with highly active and reusable is an urgent task to achieve green hydrogen production via $NaBH_4$. Herein, we proposed a novel NaCl template method, which involves solid-state physical grinding of metal salts, reducing agents and prepared carbon spheres with the participation of sodium chloride to synthesize Ru-particles decorated CoB_2O_4 supported on hollow mesoporous carbon nanospheres (Ru/CoB_2O_4@C) catalysts for efficient and durable H_2 generation through alkaline hydrolysis of $NaBH_4$. The optimized catalyst with a Ru content of 3.0 wt% exhibits a high hydrogen generation rate of 8139 mL min^{-1} g_{cat}^{-1} and a low activation energy of 33.2 kJ mol^{-1} for $NaBH_4$ hydrolysis, which is one of the most efficient catalysts reported recently. The extraordinary performance is mainly attributed to the synergistic effect between Ru and CoB_2O_4 species and abundant oxygen vacancies, which facilitate charge redistribution and provide more active sites, thereby enhancing the catalytic activity. Density functional theory calculations support the proposed Michaelis-Menten mechanism, where BH_4^- and H_2O are adsorbed on electron-rich Ru and electron-deficient CoB_2O_4 surfaces, respectively, and the reaction energy barrier for the rupture of the B-H bond as the rate-determining step is only 1.37 eV, synergistically promoting the hydrolysis of $NaBH_4$. Our study provides an innovative method for designing efficient and stable catalysts for green hydrogen generation.

1. Introduction

Hydrogen (H_2) is widely recognized as an environmentally friendly and sustainable alternative energy carrier compared to conventional fossil fuels, owing to its cleanliness and high calorific value [1]. However, the implementation of hydrogen as a widespread energy carrier is hindered by challenges in its transportation and storage [2–4]. To address these issues, borohydrides, specifically sodium borohydride ($NaBH_4$), have been identified as a promising solution due to their high hydrogen storage capacity (10.8 wt%) and excellent stability at room temperature [5,6]. Furthermore, $NaBH_4$ is widely regarded as the optimal choice for green hydrogen production due to its attractive characteristics, including renewability [7], environmental friendliness [8], and cost-effectiveness [9]. Notably, $NaBH_4$ enables product recycling through direct high-energy ball milling. The hydrogen production process associated with $NaBH_4$ does not generate greenhouse gases or pollutants, making it environmentally advantageous and aligning well with the principles of green hydrogen production. Moreover, $NaBH_4$ offers the advantage of lower raw material costs and a relatively simple manufacturing process, contributing to the overall cost reduction of hydrogen production compared to other methods. Nonetheless, the sluggish reaction kinetics of $NaBH_4$'s self-hydrolysis limit its practical use [10]. By employing an appropriate catalyst, the reaction of one equivalent of $NaBH_4$ with water can produce four equivalents of hydrogen [11,12].

It is crucial to design a durable and high-performance catalyst to develop a practice H_2 storage and reuse process. According to recent research, the most advanced catalysts for borohydrides hydrolysis currently rely heavily on noble metals such as Palladium (Pd) and Platinum (Pt) [13,14]. However, their scarcity and high cost pose a challenge to large-scale applications. As a result, non-noble metal catalysts have garnered a great deal of attention due to their lower cost [9], as well as their better activity and stability, particularly when supported on appropriate substrates [15], Nonetheless, these catalysts have limited

* Corresponding authors.
E-mail addresses: isimjant@sabic.com (T.T. Isimjan), xlyang@gxnu.edu.cn (X. Yang).

https://doi.org/10.1016/j.cej.2024.148547
Received 25 August 2023; Received in revised form 27 December 2023; Accepted 2 January 2024
Available online 4 January 2024

selectivity and are susceptible to deactivation or degradation over time, particularly in harsh reaction conditions or in the presence of impurities [16].

Boron-containing compounds are known for their favorable physical properties, including low cost, good electrical conductivity, and environmental friendliness, in comparison to transition metal oxides [17], hydroxides [18], and phosphides [19]. Moreover, boron (B) in these compounds exhibits distinctive chemical properties when compared to other common non-metal elements like sulfur (S), oxygen (O), and phosphorus (P). The B element possesses the ability to modulate the electronic structure and rearrange the electron cloud density. Meng et al. have proposed that the introduction of quasi-metallic B atoms in metal boride-based materials can effectively regulate the electronic properties of complex metal sites, providing avenues for optimizing application performance [20]. Boron, being a moderately electronegative semi-metal element, exhibits diverse types of chemical bonds in boron compounds, including ionic bonds (M-B) and covalent bonds (B-B). Due to their unique properties, structural diversity, and compositional flexibility, borates have a strong capacity to regulate the adsorption capacity and local electronic structure of active sites on catalyst surfaces. These characteristics create favorable conditions for the modification of redox catalysts [21]. In recent studies, the addition of a small amount of ruthenium (Ru) to the $NaBH_4$ catalyst has been shown to offer several advantages in chemical reactions [22]. The presence of Ru on the catalyst surface can improve its catalytic activity, selectivity, and stability, resulting in faster reaction rates, higher yields, and reduced catalyst deactivation [23,24].

In addition to the chemical composition of a catalyst, its performance is also significantly affected by the catalyst support material used [25]. Proper supports, such as carbon nanotubes [26], nickel foam [18,27], and hollow carbon spheres [28], can improve metal dispersion, reduce the amount of precious metals, decrease costs, enhance catalytic activity, and prolong the catalyst's lifetime. Among these options, hollow mesoporous carbon nanospheres are an excellent support material due to their exceptional porosity, structural diversity, and large specific surface area [29,30]. As a result, they have become a preferred substrate for loading active ingredients [31], providing ample active sites and facilitating the release of gases during $NaBH_4$ hydrolysis. Incorporating low-loading of highly catalytic noble metals such as ruthenium (Ru) into supported catalytic systems can not only improve catalytic activity, stability, and reusability but also effectively reduce costs [32]. Furthermore, the NaCl template method can be employed during the synthesis process to achieve a more uniform metal dispersion on the surface of carbon spheres, prevent agglomeration, and enhance the catalyst's performance [33].

In this work, we present an efficient and controlled approach to synthesize Ru-particles decorated CoB_2O_4 on carbon sphere (Ru/CoB_2O_4@C) for catalytic hydrolysis of sodium borohydride in alkaline environments. The interaction between Ru and Co species is induced by CoB_2O_4 innovation, which results in strong electronic interaction. DFT calculations reveal that electron interaction between Ru and CoB_2O_4 can facilitate charge transfer, leading to fast reaction kinetics. The exceptional hollow mesoporous structure of the catalyst creates a suitable three-phase interface that promotes the reaction by providing a larger specific surface area, reducing diffusion resistance, and exposing a high density of active sites. Therefore, the optimized Ru/CoB_2O_4@C catalyst exhibits outstanding activity in alkaline sodium borohydride solution, indicating its potential for application in energy storage and conversion processes.

2. Experimental sections

2.1. Materials

Ethanol ($C_2H_5OH \geq 99.7$ %), formaldehyde solution (HCHO, 37.0 wt %), tetraethyl silicate (TEOS ≥ 28.0 %), resorcinol ($C_6H_6O_2 \geq 99.5$ %), cobalt chloride hexahydrate ($CoCl_2{\cdot}6H_2O$, 98 %) ammonium hydroxide (NH_4OH, 25.0 wt%), sodium hydroxide (NaOH, 96 %), and sodium borohydride ($NaBH_4 \geq 98.0$ %) were purchased from Xilong Chemical Co., Ltd. Ruthenium(III) chloride hydrate ($RuCl_3{\cdot}xH_2O$) was got from Aladdin Industrial Corporation. All chemicals and reagents were of analytical grade and used directly without further purification.

2.2. Synthesis of carbon spheres

The procedure for obtaining the hollow mesoporous carbon spheres substrate was adapted from previous work [34]. Briefly, 3.5 mL of TEOS was added to a stirred mixed solution containing 10 mL deionized water, 50 mL ethanol, and 2 mL NH_4OH. After 10 min, 0.5 mL of formaldehyde solution and 3.54 mmol $C_6H_6O_2$ were added sequentially. The mixture was then vigorously stirred at room temperature for 24 h before being centrifuged at 8000 rpm for 10 min to obtain solid brown powder. The powder was washed with ethanol three times and dried in an oven at 70 °C.

The resulting brown powder was then annealed at 700 °C for 5 h in a nitrogen atmosphere with a ramping rate of 5 °C min^{-1} to obtain SiO_2@C. Finally, the SiO_2 core was removed by soaking the sample in 3 M KOH at 60 °C overnight to obtain the hollow mesoporous carbon spheres.

2.3. Synthesis of Ru/CoB_2O_4@C

During the synthesis, 30 mg of carbon spheres were dispersed in a solution containing 0.13 mmol $CoCl_2{\cdot}6H_2O$ and 0.04 mmol $RuCl_3{\cdot}xH_2O$ in 15 mL of ethanol. The mixture was ultrasonicated for 1 h, and then transferred to a vacuum oven at 70 °C overnight to allow complete evaporation of the ethanol. The remaining black powder was scraped off and set aside.

The powder was ground together with 17 mmol of NaCl and 16.7 mmol of CH_4N_2O, transferred to a clean beaker, and dried in an oven for 4 h. The dried precursor was mixed with 2.6 mmol of $NaBH_4$ and thoroughly ground in an agate mortar to ensure complete solid-state reaction. The catalyst was separated by centrifugation, washed with deionized water several times, and dried overnight at 70 °C. To compare the performance of different Ru doping levels, the Ru/Co molar ratio was varied (1:2, 1:3, 1:4, 1:5) during the synthesis process.

2.4. Synthesis of CoB_2O_4@C and Ru@C

The CoB_2O_4@C and Ru@C catalysts were prepared using a similar method as described for Ru/CoB_2O_4@C above, with the exception that only $CoCl_2{\cdot}6H_2O$ or $RuCl_3{\cdot}xH_2O$ were added during the synthesis.

2.5. Synthesis of Pt/CoB_2O_4@C, Pd/CoB_2O_4@C and Rh/CoB_2O_4@C

The synthesis protocol mirrors that employed for Ru/CoB_2O_4@C, with the sole variation being the substitution of $RuCl_3$ xH_2O with the relevant precious metal salts.

2.6. Catalytic measurements

The catalytic activity, cycle stability and activation energy of the catalytic material were obtained by the following methods. Typically, 25 mL mixture solution (contained 150 mM $NaBH_4$ + 0.4 wt% NaOH) was kept in a three-necked round-bottom flask (50 mL), which was placed in a water bath at 25 °C. The volume of H_2 was monitored by a drainage which was connected to a computer to record the instantly changed water quantity. The catalytic reaction was started when the catalyst was added into the flask under constant magnetic stirring conditions. In order to test the recyclability of the catalyst, we continued to use the fresh $NaBH_4$ solution instead of the fully decomposed $NaBH_4$ solution for five consecutive cycles at 25 °C. After each stability test, we

centrifuged the catalytic material, dried it under vacuum condition at room temperature, and weighed the catalytic material. All performance tests were conducted three times under identical conditions, and the experimental results were averaged to ensure accuracy. The activation energy of the designed catalyst was evaluated in the same device in the temperature range of 25–45 °C.

3. Results and discussion

3.1. Structural and morphological characterizations

The Ru/CoB_2O_4@C catalyst was prepared through a series of steps including impregnation, NaCl template regulation, and chemical reduction method to load the Ru/CoB_2O_4 onto hollow porous nanospheres, as depicted in Fig. 1a. Initially, a quantity of carbon spheres were submerged in an ethanol solution containing $CoCl_2{\cdot}6H_2O$ and $RuCl_3{\cdot}xH_2O$ to uniformly coat them with Co and Ru species. Subsequently, the mentioned precursors were combined with NaCl and CH_4N_2O for a solid-state reaction. Upon mixing and grinding all the materials, CoB_2O_4 nucleates on the surface of the water-soluble NaCl particles, which possess a face-centered cubic crystal structure, within an agate mortar. This nucleation process leads to the aggregation of CoB_2O_4 along the cubic crystal structure. As a result, the assembled 3D structure comprising small particles of CoB_2O_4 can be easily obtained by removing NaCl using distilled water [35]. Finally, the Ru particles were reduced onto the CoB_2O_4@C (Ru/CoB_2O_4@C) via $NaBH_4$.

The crystalline characteristics of the prepared catalysts were analyzed by X-ray diffraction (XRD) patterns, which showed a broad peak at around 22.0° belonging to (0 0 2) facets of graphitic carbon [36], and diffraction peaks at around 31.0°, 36.8°, 44.6°, 59.2°, and 65.2° assigned to CoB_2O_4 (JCPDS: 01–1145) [21]. The diffraction peak of Ru in the spectrum was not prominent due to its low-loadings, except for the peak attributed to the (1 0 1) crystal plane, which was around 44.0° (Fig. 1b) [37]. This particular observation was consistent across pure Ru, CoB_2O_4@C, and Ru/Co catalysts with different ratios (**Fig. S1**). The Ru content on the Ru/CoB_2O_4@C was found to be 3.0 wt% tested by inductively coupled plasma mass spectroscopy (ICP-MS) (Table S1). Electron paramagnetic resonance (EPR) spectra demonstrated that the signal intensity of the broad signal, which serves as an evaluation index for the degree of vacancies in the composite, was stronger in Ru@C compared to Ru/CoB_2O_4@C, indicating that the Co species occupied some of the oxygen vacancies [32]. The Co^{2+} ions, converted to Co^{3+} through a process involving electron deficiency created by oxygen vacancies, occupy some of the oxygen vacancies in the composite. However, the introduction of oxygen vacancies altered the electronic properties of Ru/CoB_2O_4@C, enhancing the catalytic activity [38,39]. The N_2 adsorption–desorption isotherm demonstrated a reversible IV-type isotherm with an evident hysteresis loop, indicating the mesoporous structure of Ru/CoB_2O_4@C (Fig. 1d) [40,41]. Comparative samples, such as Ru@C and CoB_2O_4@C, mirrored these structural traits (**Fig. S2**). BET analyses determined specific surface areas of 2316.5 $m^2\ g^{-1}$ for CoB_2O_4@C, 217.2 $m^2\ g^{-1}$ for Ru@C and 328.1 $m^2\ g^{-1}$ for Ru/CoB_2O_4@C. This data suggests that the presence of Ru obstructed some of the surface areas of the CoB_2O_4. Such observations echo findings from recent scholarly articles [42,43]. The superior data were attributed to the hollow structure of carbon nanospheres, which facilitated the exposure of active sites in the catalytic process [44]. Furthermore, the presence of mesopores of approximately 9.3 nm on the surface of the carbon spheres prevented Ru and CoB_2O_4 NPs from stacking and facilitated gas transport, increasing the catalytic rate at the active site (inset in Fig. 1d) [45]. Raman spectroscopy was employed to gauge the degree of carbon disorder, attributable to the carbon carriers, via the intensity ratio of the D band to the G band (I_D/I_G). (Fig. S3a). The I_D/I_G values for Ru/CoB_2O_4@C, CoB_2O_4@C and Ru@C are 0.98, 0.97 and 0.96, respectively. This consistency suggests that the surface disorder induced by the metal loading is fairly uniform across samples. Notably, the B-O stretching vibration is represented by the peak at 903 cm^{-1} [46]. The Fourier Transform Infrared (FTIR) spectra for Ru/CoB_2O_4@C, CoB_2O_4@C and Ru@, spanning the wavenumber range of 500–4000 cm^{-1}, are depicted in Fig. S3b. The bands discerned at around 704 and 1250 cm^{-1} are mainly due to Ru-O bond and B-O bond in RuO_2 and $B_2O_4^{2-}$, respectively [47,48]. The thermodynamic stability of samples was detected in **Fig. S4**.

The morphology of material was examined using scanning electron microscopy (SEM) and transmission electron microscopy (TEM). The SiO_2@C material had a smooth, spherical structure, whereas the surface of the carbon spheres became rough and porous after etching with alkaline KOH solution (**Fig. S5**). As shown in Fig. 2a-b, the Ru/CoB_2O_4

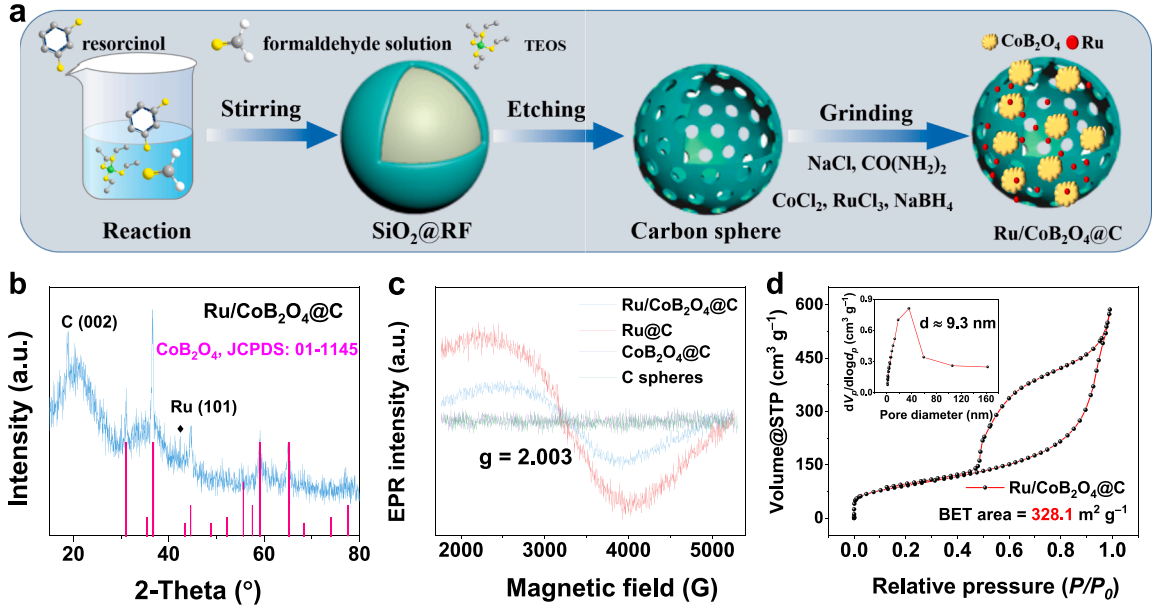

Fig. 1. (a) Schematic illustration of preparation Ru/CoB_2O_4@C. (b) XRD patterns of Ru/CoB_2O_4@C. (c) EPR spectra of Ru/CoB_2O_4@C, CoB_2O_4@C, Ru@C and carbon spheres. (d) N_2 adsorption–desorption isotherm with the inset showing the corresponding pore size distribution of Ru/CoB_2O_4@C.

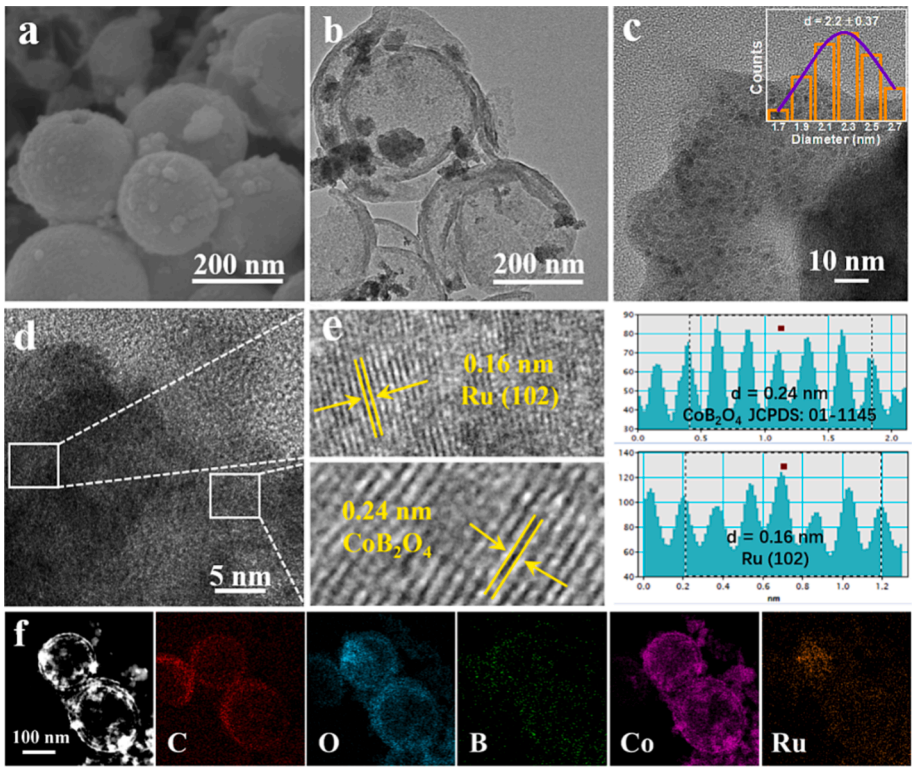

Fig. 2. (a) SEM and (b) TEM image of Ru/CoB_2O_4@C, (c) TEM (histogram of particle size distribution of Ru particles on catalyst surface). (d-e) HR-TEM and the corresponding lattice spacing profiles of the dotted line regions. (f) HAADF-STEM images and the corresponding elemental mappings of Ru/CoB_2O_4@C.

catalyst was uniformly dispersed on the surface of the hollow mesoporous carbon spheres, forming a particulate structure (Ru/CoB_2O_4@C). This dispersion helped to mitigate the performance degradation caused by CoB_2O_4 agglomeration to some extent. As shown in Fig. 2c, the Ru particles with an average particle size of about 2.20 nm, as determined from statistical analysis of a significant number of Ru particles, are uniformly dispersed on the CoB_2O_4 (the inset presents the histogram of the Ru particle size distribution). High-resolution TEM (HR-TEM) images showed lattice fringes of Ru/CoB_2O_4@C (Fig. 2d-e), with a spacing of 0.16 nm corresponding to the (1 0 2) crystal plane of Ru [49], and a spacing of 0.24 nm belonging to CoB_2O_4 species [21]. The presence of Ru and CoB_2O_4 in the Ru/CoB_2O_4@C composite is further corroborated by the selected area electron diffraction (SAED) pattern (**Fig. S6**). The pronounced diffraction spots predominantly correspond to the CoB_2O_4 and Ru (1 0 2) phases. The energy dispersive X-ray (EDX) spectrum shows Co, Ru, B, O and C signals in Ru/CoB_2O_4@C (**Fig. S7**). Furthermore, high-angle annular dark-field scanning transmission electron microscopy (HAADF-STEM) confirmed the presence of the hollow mesoporous structure, and corresponding element mappings demonstrated even distribution of C, O, B, Co, and Ru on the surface of Ru/CoB_2O_4@C (Fig. 2f).

X-ray photoelectron spectroscopy (XPS) was utilized to examine the chemical states and composition of elements. The survey XPS spectra (**Fig. S8a**) indicated that the catalysts were mainly composed of Co, O, C, Ru, and B elements. The high-resolution C 1 *s* + Ru 3*d* spectra were deconvoluted into four peaks at 284.0, 284.8, 286.0, and 288.65 eV, which were indexed as C = C, C − C, C − O and C = O, respectively [50]. The Ru 3*d* XPS spectrum of Ru/CoB_2O_4@C revealed peaks at approximately 279.9 and 284.1 eV, denoting metallic Ru^0. Conversely, peaks at 280.9 eV and 285.1 eV can be attributed to RuO_2 (Fig. 3a) [51]. The Ru

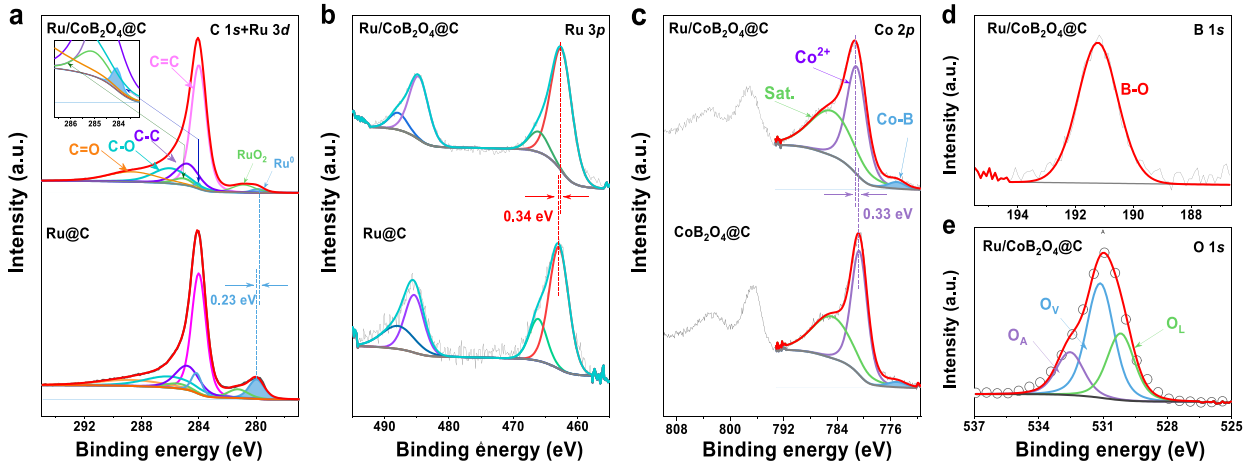

Fig. 3. High-resolution XPS spectra of (a) C 1 *s* + Ru 3*d*, (b) Ru 3*p*, (c) Co 2*p*, (d) B 1 *s* and (e) O 1 *s* regions of Ru/CoB_2O_4@C, Ru@C and CoB_2O_4@C.

3*p* spectrum (Fig. 3b) showcased two sets of peaks: those centered at 462.7 and 484.9 eV correspond to Ru $3p_{3/2}$ and Ru $3p_{1/2}$, respectively. The secondary peaks at 466.3 and 487.9 eV are linked to RuO_2 $3p_{3/2}$ and RuO_2 $3p_{1/2}$. These are likely the result of Ru surface oxidation during catalyst preparation [52]. The binding energies of Ru^0 in both the 3*d* and 3*p* orbitals were found to shift negatively by 0.23 eV and 0.34 eV, respectively, in comparison to Ru@C. The Co 2*p* spectrum of Ru/CoB_2O_4@C (Fig. 3c) was fitted into three peaks: Co-B (775.1 eV), Co-O (781.3 eV), and satellite (785.2 eV) [53,54]. The binding energy of Co-O was positively shifted by 0.33 eV in comparison to CoB_2O_4@C, indicating that electrons were transferred from Co^{2+} to Ru, which resulted in enhanced hydrolysis activity [55,56]. The interaction generated by charge redistribution was noteworthy. The B 1 *s* peak for Ru/CoB_2O_4@C, observed at 191.2 eV, corresponds to B^{3+} in borate (Fig. 3d). The O 1 *s* spectrum exhibited three prominent peaks at 530.2, 531.1 and 532.5 eV, which could be assigned to lattice oxygen (O_L), oxygen vacancy (O_v) and absorbed oxygen (O_A), respectively. The presence of strong O_v peaks was consistent with the EPR results (Fig. 3e) [57]. Furthermore, the high-resolution C 1 *s* and B 1 *s* spectra of CoB_2O_4@C were presented in **Fig. S8b-c**, and they exhibited similar bonding states to Ru/CoB_2O_4@C.

3.2. $NaBH_4$ hydrolysis performance

Hydrogen generation via the hydrolysis of $NaBH_4$ was carried out in an alkaline environment at 25 °C, and the amount of hydrogen produced was determined using the drainage method (**Fig. S9**). To avoid the autohydrolysis of $NaBH_4$ (**Fig. S10a**), NaOH was used as a stabilizing agent to achieve controlled hydrolysis, which only occurs under the catalytic action (**Fig. S10b**). Furthermore, we explored the relationship between different NaOH concentrations and the hydrogen generation rate (**Fig. S10c**). Interestingly, we found that the hydrogen generation rate was minimally affected by the NaOH concentration, consistent with previous reports [32]. As a result, we selected 0.4 wt% NaOH, in accordance with the principles of green chemistry, as the stabilizer for the hydrolysis process. The effect of different molar ratios of Ru and Co in the catalyst preparation was investigated to optimize the catalytic performance for sodium borohydride hydrolysis. The catalyst exhibited the best performance when the Ru:Co ratio was 1:3 (Fig. 4a). The catalyst's hydrogen generation rate and turnover frequency displayed a volcano-like trend based on varying ratios of the two metals. Peak values reached 8139 mL min^{-1} g_{cat}^{-1} and 82 mol_{H2} min^{-1} mol_M^{-1}, as illustrated in Fig. 4b. The Ru content in Ru/CoB_2O_4@C was a mere 3.0 wt%, which is comparatively lower than many analogous catalysts reported in references [58,59]. This parameter was kept constant during the rest of the optimization process. It is evident that the catalytic activity of sodium borohydride hydrolysis of Ru/CoB_2O_4@C is much superior to all other control samples (Fig. 4c). The TOF values of Ru / CoB_2O_4@C, CoB_2O_4@C, and Ru@C are fully presented in Fig. 4d and **Table S2**, and the catalyst also outperforms most of the previously reported catalysts (**Table S3**). At the same time, we also explored the catalytic activities of different noble metals, including Pt, Pd and Rh, under the same reaction conditions. As shown in **Fig. S11**, while the efficacy of our target catalyst, Ru/CoB_2O_4@C, marginally trails that of Pt/CoB_2O_4@C, it surpasses the performances of both Pd/CoB_2O_4@C and Rh/CoB_2O_4@C. Given the economic implications tied to the catalyst's cost, a catalyst with a low loading of the more affordable noble metal Ru emerges as the most judicious choice.

The effect of temperature on the hydrolysis of catalytic $NaBH_4$ was investigated by measuring the catalytic performance of Ru/CoB_2O_4@C and Ru@C under different conditions. The results showed that the generation rate of H_2 increased significantly with increasing hydrolysis temperature (Fig. 5a and **Fig. S12**). The activation energy of Ru/CoB_2O_4@C was calculated to be 33.2 kJ mol^{-1}, which was superior to that of Ru@C (42.3 kJ mol^{-1}) and most of the previously reported catalysts (Fig. 5b-c), indicating excellent catalytic performance of Ru/CoB_2O_4@C. Furthermore, the reusability capacity of Ru/CoB_2O_4@C for catalytic hydrogen production was demonstrated to be superior, with 90.7 % of its initial activity retained after the fifth cycle (Fig. 5d and Fig. 5e). This excellent reuse stability is superior to most previously reported catalysts (Fig. 5f). However, a slight decline in catalytic performance was observed, which was mainly attributed to the poisoning of active sites by the generated BO_2^- [10,60], as well as the agglomeration and exfoliation of catalytically active components (**Table S4**).

To gauge the robustness and endurance of the catalyst during the reaction, the spent Ru/CoB_2O_4@C catalyst, post five cycles, underwent meticulous examination using SEM, TEM, XRD, and XPS techniques. SEM images illustrated that the morphology of the spent catalyst

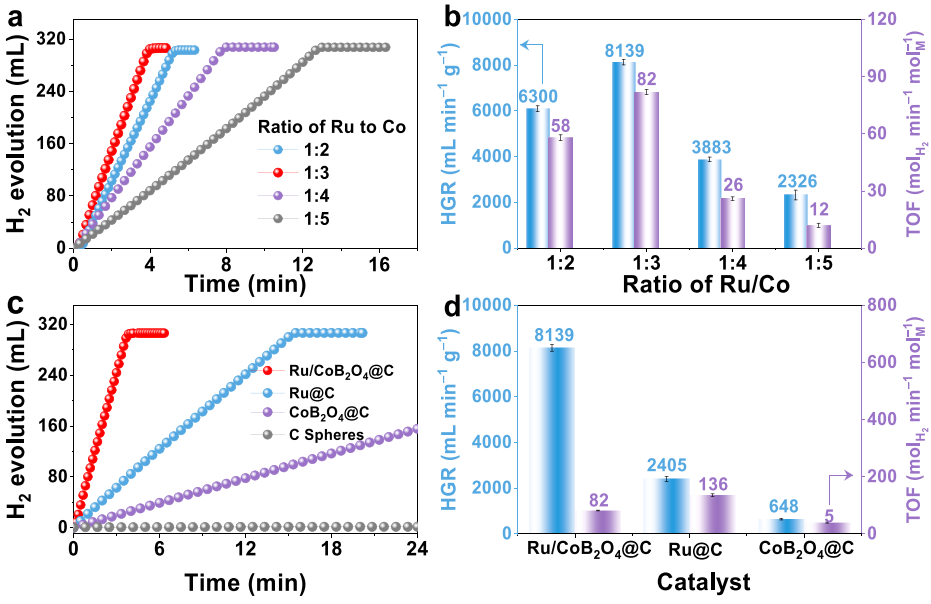

Fig. 4. (a) Stoichiometric H_2 evolution in 150 mM $NaBH_4$ + 0.4 wt% NaOH solution by Ru/CoB_2O_4@C catalysts with different ratio of Ru to Co at 25 °C, and (b) the corresponding H_2 evolution rate values and TOF values. (c) H_2 evolution by different catalysts at 25 °C, and (d) the summarized H_2 evolution rate values and TOF values.

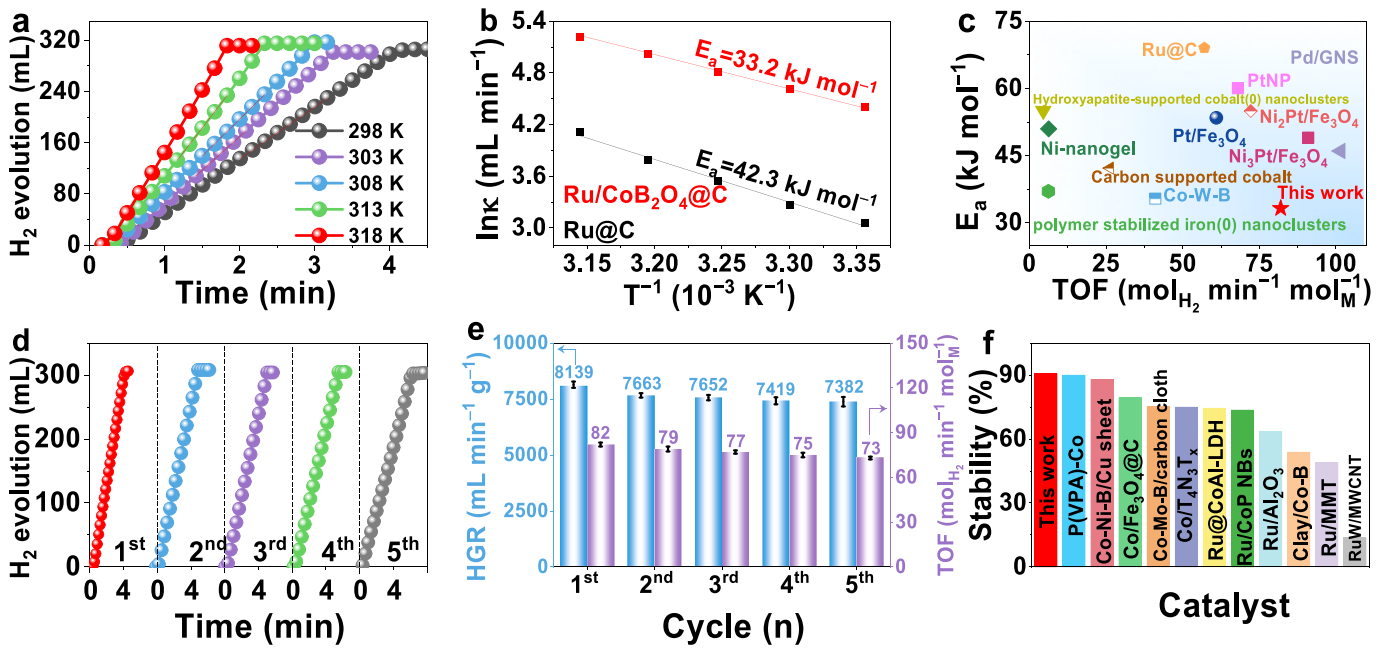

Fig. 5. (a) The relationship between the H_2 generation rate and applied temperatures of Ru/CoB_2O_4@C. (b) Arrhenius plots of Ru/CoB_2O_4@C and Ru@C. (c) Comparison of the hydrolysis performance of Ru/CoB_2O_4@C with other recently reported catalysts. (d) Recycling stability test of Ru/CoB_2O_4@C catalyst in 150 mM $NaBH_4$ + 0.4 wt% NaOH at 25 °C. (e) Corresponding H_2 evolution rate values and TOF values in different recycling tests. (f) Stability of catalysts involved in recently published work.

predominantly mirrored its original state, albeit with minor damage observed on a few carbon spheres-a plausible consequence of gas evolution during the reaction (**Fig. S13a**). Insightful observations from TEM and XRD highlighted that the catalytic components were consistently distributed across the catalyst's surface, and the crystalline nature of the material remained largely unaltered, emphasizing the inherent stability of the catalyst (**Fig. S13b-c**). Furthermore, the EDX analysis substantiated the continued presence of Co, Ru, B, O, and C elements in the spent Ru/CoB_2O_4@C catalyst (**Fig. S13d**). XPS qualitative analysis indicated that the original elemental composition of the catalyst was retained after catalytic hydrolysis, demonstrating its stability (**Fig. S14**) [61]. It is noteworthy that the proportion of metallic Ru on the catalyst surface slightly increased from 42.5 % to 55.1 % due to the reduction of $NaBH_4$, while the Ru content decreased from 3.0 wt% to 2.1 wt% after five cycles due to Ru exfoliation. A small amount of metal (Co, Ru) was detected in the reaction solution after circulation, which further confirmed the exfoliation of the material (**Table S4**).

3.3. DFT calculations and catalytic mechanism analysis

Density functional theory (DFT) calculations were performed to investigate the potential mechanism of hydrogen production from $NaBH_4$ catalyzed by Ru/CoB_2O_4@C catalyst. Our calculations showed an electron accumulation at the edge of Ru and electron deficiency around Co species, which corroborates the XPS results and confirms a charge synergy between Ru and Co species (Fig. 6a). We also evaluated the Bader charges of Ru and Co atoms on various catalysts to determine the adsorption sites for BH_4^- and H_2O (Fig. 6b). Our data indicated that the Ru/CoB_2O_4@C catalyst, containing Ru and Co, exhibited the highest electron affinity and lowest electron deficiency compared to other investigated catalysts. Consequently, a high molar [BH_4^-]/[Ru] ratio facilitates the removal of H^- ions from BH_4^- ions by electron transfer from the BH_4^- ions through Ru/CoB_2O_4. Meanwhile, H–OH bonds of the H_2O absorbed on the surface of CoB_2O_4 are weakened, favoring the reduction of H^+ through the transferred electron from BH_4^- ions. The combination of H^+ and H^- immediately leads to the liberation of H_2 (**Fig. S15**) [60].

Two mechanisms are widely recognized for the catalytic hydrolysis of $NaBH_4$, namely the Langmuir-Hinshelwood and the Michaelis-Menten mechanisms (**Fig. S16**, Fig. 6e) [62,63]. Based on these mechanisms, we calculated the adsorption energy required for each step in the catalytic hydrolysis process of Ru/CoB_2O_4@C. As shown in Fig. 6c, the energy required for the rate-determining step in the Michaelis–Menten mechanism is 1.37 eV, which is less than 2.62 eV in the Langmuir-Hinshelwood mechanism. Therefore, we concluded that Ru/CoB_2O_4@C follows the Michaelis-Menten mechanism when catalyzing the hydrolysis of $NaBH_4$ to produce H_2.

$$*BH_4^- \rightleftharpoons *BH_3 + *H^- \quad (1)$$

$$*H^- + H_2O \rightleftharpoons H_2 + *OH^- \quad (2)$$

$$*OH^- + *BH_3 \rightleftharpoons *BH_3OH^- \quad (3)$$

$$*OH^- + *BH(OH)_3 \rightleftharpoons B(OH)_4 \quad (4)$$

To better understand the kinetics of the $NaBH_4$ hydrolysis reaction, the reaction barriers of various catalysts for each elementary step were calculated, including the barriers for the adsorption of BH_4^- and H_2O and the dissociation energies of the products (Fig. 6d). Previous reports have indicated that the breaking of the B-H bond in the hydrolysis is likely the rate-determining step [64], which is consistent with the reaction process represented by ΔG_4. Accordingly, the energy barrier (ΔG_4) for the rate-determining step in the Ru/CoB_2O_4@C catalyst was determined to be 1.37 eV, which is lower than that of Ru@C (1.84 eV) and CoB_2O_4@C (1.97 eV). This indicates that Ru/CoB_2O_4@C facilitates the formation of transition state intermediates and promotes the hydrolysis reaction kinetics of sodium borohydride (**Table S5**). Based on the experimental and theoretical results, a proposed alkaline hydrolysis mechanism for the Ru/CoB_2O_4@C catalyst is illustrated in Fig. 6e: (I) BH_4^- is adsorbed on the surface of Ru sites in the Ru/CoB_2O_4 catalyst; (II) the B–H bond of $*BH_4^-$ dissociates at the Ru metal sites, producing $*H^-$ and $*BH_3$, along with electron transfer (Eq. (1)); (III) to facilitate the hydrolysis process, H_2O is adsorbed on the surface of the Co species of the catalyst; (IV) the $*H^-$ on the Ru surface interacts with one of the protonic H^+ of H_2O, resulting in the release of one molecule of H_2 (Eq. (2)), and the

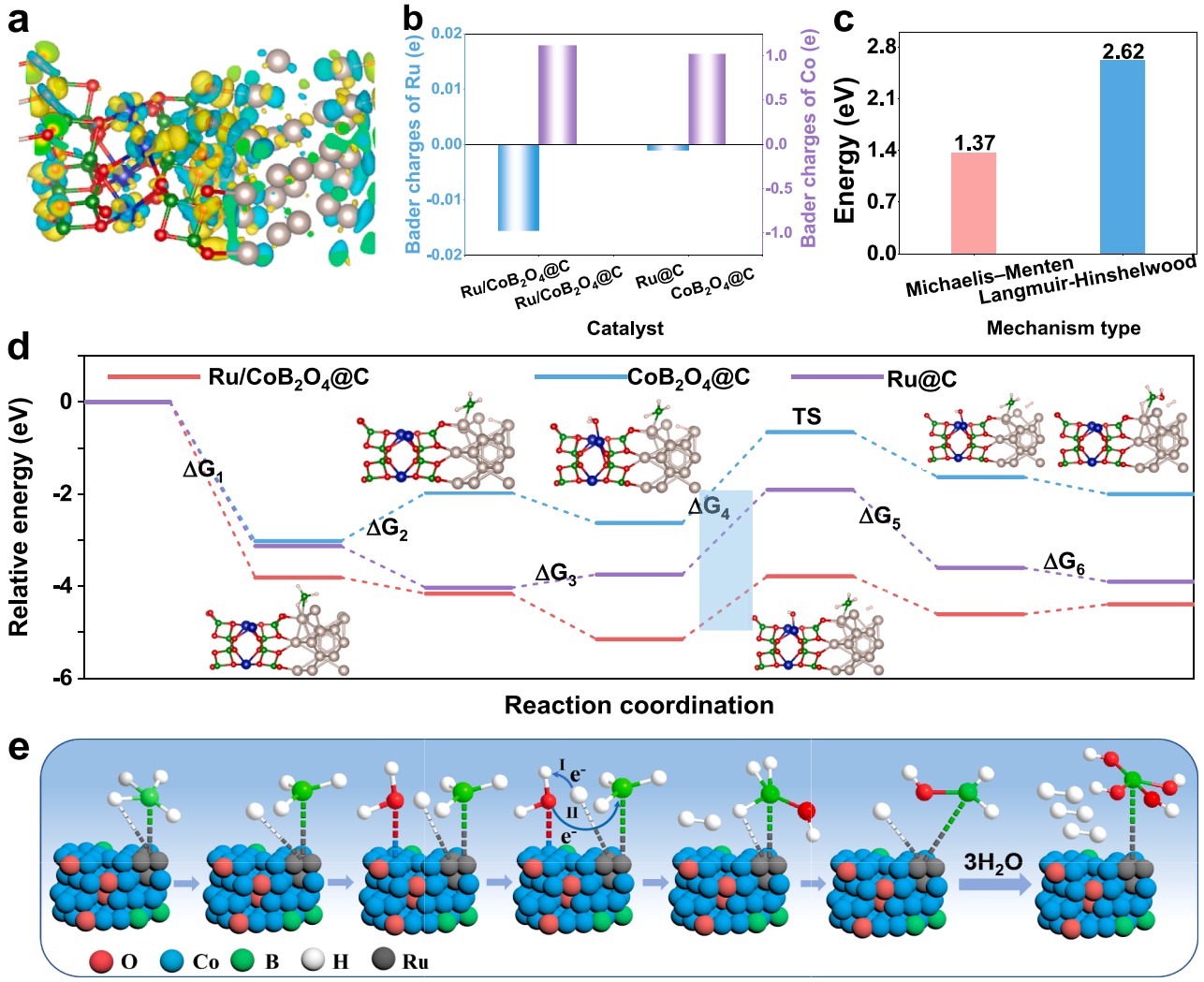

Fig. 6. (a) The charge density difference of $Ru/CoB_2O_4@C$ model. Yellow and green region depict electron accumulation and depletion, respectively. (b) Bader charges of Ru and Co atoms on $Ru/CoB_2O_4@C$, Ru@C and $CoB_2O_4@C$ catalysts. (c) The energies corresponding to the rate-determining steps of different mechanisms on $Ru/CoB_2O_4@C$ catalyst. (d)The free energy curves of $Ru/CoB_2O_4@C$, Ru@C and $CoB_2O_4@C$ for the catalytic hydrolysis of $NaBH_4$. (e) Schematic representation of the Michaelis-Menten mechanism.

remaining $*OH^-$ combines with adsorbed $*BH_3$ to form $*BH_3OH^-$ (Eq. (3)); and (V) the H in BH_3OH^- generated in the previous step continues to adsorb onto Ru, similar to step (I). Through the involvement of Ru/CoB_2O_4, this cycle ultimately produces four hydrogen molecules and tetrahydroxyboronic acid $B(OH)_4^-$ as the end-product from a single BH_4^- molecule and H_2O (Eq. (4)) [61].

4. Conclusions

In summary, we have demonstrated a novel NaCl template strategy to induce hydrolysis of borohydride using Ru/CoB_2O_4 modified hollow mesoporous carbon nanospheres at room temperature. The optimized $Ru/CoB_2O_4@C$ composite exhibits excellent hydrolysis of $NaBH_4$ activity, with a hydrogen generation rate of 8139 mL min^{-1} g_{cat}^{-1}, surpassing that of recently reported transition metal-based catalysts. XPS analysis shows that the superior $NaBH_4$ hydrolysis performance is attributed to the strong synergistic effect between Ru and CoB_2O_4 species. Moreover, TEM and BET characterizations confirm that the hollow mesopores structure with high specific surface area of $Ru/CoB_2O_4@C$ can expose a high density of active sites, facilitating gas transport and accelerating reaction kinetics. The TOF value can reach 82 mol_{H2} min^{-1} mol_M^{-1}, and the catalyst exhibits superior reusability, with no significant decay in catalytic performance after five cycles. These results demonstrate the promising potential of $Ru/CoB_2O_4@C$ for $NaBH_4$ hydrolysis applications.

CRediT authorship contribution statement

Huatong Li: Investigation, Writing – original draft, Data curation. **Xinran Hu:** Investigation. **Lixia Wang:** Data curation. **Luyan Shi:** Investigation, Methodology. **Tayirjan Taylor Isimjan:** Writing – review & editing. **Xiulin Yang:** Supervision, Writing – review & editing.

Declaration of competing interest

The authors declare that they have no known competing financial interests or personal relationships that could have appeared to influence the work reported in this paper.

Data availability

The data that has been used is confidential.

Acknowledgements

This work has been supported by the National Natural Science Foundation of China (no. 52363028, 21965005), Natural Science Foundation of Guangxi Province (2018GXNSFAA294077, 2021GXNSFAA076001), Innovation Project of Guangxi Graduate Education (YCSW2023140) and Guangxi Technology Base and Talent Subject (GUIKE AD18126001, GUIKE AD20297039).

Appendix A. Supplementary data

Supplementary data to this article can be found online at https://doi.org/10.1016/j.cej.2024.148547.

References

[1] H. Zhang, L. Zhang, I.A. Rodríguez-Pérez, W. Miao, K. Chen, W. Wang, Y. Li, S. Han, Carbon nanospheres supported bimetallic Pt-Co as an efficient catalyst for $NaBH_4$ hydrolysis, Appl. Surf. Sci. 540 (2021) 148296, https://doi.org/10.1016/j.apsusc.2020.148296.

[2] M. Allendorf, V. Stavila, J. Snider, M. Witman, M. Bowden, K. Brooks, B. Tran, T. Autrey, Challenges to developing materials for the transport and storage of hydrogen, Nat. Chem. 14 (2022) 1214–1223, https://doi.org/10.1038/s41557-022-01056-2.

[3] Y. Liu, Q. Wang, J. Zhang, J. Ding, Y. Cheng, T. Wang, J. Li, F. Hu, H.B. Yang, B. Liu, Recent advances in carbon-supported noble-metal electrocatalysts for hydrogen evolution reaction: syntheses, structures, and properties, Adv. Energy Mater. 12 (2022) 2200928, https://doi.org/10.1002/aenm.202200928.

[4] E. Pawelczyk, N. Łukasik, I. Wysocka, A. Rogala, J. Gębicki, Recent progress on hydrogen storage and production using chemical hydrogen carriers, Energies 15 (2022) 4964, https://doi.org/10.3390/en15144964.

[5] J. Guo, C. Wu, J. Zhang, P. Yan, J. Tian, X. Shen, T.T. Isimjan, X. Yang, Hierarchically structured rugae-like RuP_3-CoP arrays as robust catalysts synergistically promoting hydrogen generation, J. Mater. Chem. A 7 (2019) 8865–8872, https://doi.org/10.1039/c8ta10695a.

[6] Y. Wang, J. Shen, H. Tian, X. Liu, Y. Huang, On-demand hydrogen evolution upon magnetic composite-nanocatalyzed sodium borohydride hydrolysis, J. Mol. Liq. 338 (2021) 116633, https://doi.org/10.1016/j.molliq.2021.116633.

[7] C. Qin, L. Ouyang, H. Wang, J. Liu, H. Shao, M. Zhu, Regulation of high-efficient regeneration of sodium borohydride by magnesium-aluminum alloy, Int. J. Hydrogen Energy 44 (2019) 29108–29115, https://doi.org/10.1016/j.ijhydene.2019.05.010.

[8] J.M.V. Nsanzimana, L. Gong, R. Dangol, V. Reddu, V. Jose, B.Y. Xia, Q. Yan, J. M. Lee, X. Wang, Tailoring of metal boride morphology via anion for efficient water oxidation, Adv. Energy Mater. 9 (2019) 1901503, https://doi.org/10.1002/aenm.201901503.

[9] H.N. Abdelhamid, A review on hydrogen generation from the hydrolysis of sodium borohydride, Int. J. Hydrogen Energy 46 (2021) 726–765, https://doi.org/10.1016/j.ijhydene.2020.09.186.

[10] J. Guo, B. Wang, D. Yang, Z. Wan, P. Yan, J. Tian, T.T. Isimjan, X. Yang, Rugae-like Ni_2P-CoP nanoarrays as a bi-functional catalyst for hydrogen generation: $NaBH_4$ hydrolysis and water reduction, Appl. Catal. B Environ. 265 (2020) 118584, https://doi.org/10.1016/j.apcatb.2019.118584.

[11] N. Zhang, F. Chen, X. Wu, Q. Wang, A. Qaseem, Z. Xia, The activity origin of core-shell and alloy AgCu bimetallic nanoparticles for the oxygen reduction reaction, J. Mater. Chem. A 5 (2017) 7043–7054, https://doi.org/10.1039/c6ta10948a.

[12] M. Paladini, G.M. Arzac, V. Godinho, M.C.J. De Haro, A. Fernandez, Supported Co catalysts prepared as thin films by magnetron sputtering for sodium borohydride and ammonia borane hydrolysis, Appl. Catal. B Environ. 158 (2014) 400–409, https://doi.org/10.1016/j.apcatb.2014.04.047.

[13] H. Zhang, Q. Wei, G. Wu, S. Qiu, Y. Zou, Y. Xia, F. Xu, L. Sun, H. Chu, Zn-MOF-74-derived graphene nanosheets supporting CoB alloys for promoting hydrolytic dehydrogenation of sodium borohydride, J. Alloys Compd. 930 (2023) 167486, https://doi.org/10.1016/j.jallcom.2022.167486.

[14] S. Dou, C. Hu, L. Shi, W. Zhang, S. Zhou, P. Yan, L. D'Souza, T.T. Isimjan, X. Yang, Well-dispersed Ru-clusters decorating nanobox-structured CoP synergistically catalyze the $NaBH_4$ hydrolysis and electro-reductive H_2 evolution, ChemCatChem 13 (2021) 3628–3635, https://doi.org/10.1002/cctc.202100768.

[15] K. Narasimharao, B.M. Abu-Zied, S.Y. Alfaifi, Cobalt oxide supported multi wall carbon nanotube catalysts for hydrogen production via sodium borohydride hydrolysis, Int. J. Hydrogen Energy 46 (2021) 6404–6418, https://doi.org/10.1016/j.ijhydene.2020.11.112.

[16] C. Luo, F. Fu, X. Yang, J. Wei, C. Wang, J. Zhu, D. Huang, D. Astruc, P. Zhao, Highly efficient and selective Co@ZIF-8 nanocatalyst for hydrogen release from sodium borohydride hydrolysis, ChemCatChem 11 (2019) 1643–1649, https://doi.org/10.1002/cctc.201900051.

[17] C. Wu, J. Guo, J. Zhang, Y. Zhao, J. Tian, T.T. Isimjan, X. Yang, Palladium nanoclusters decorated partially decomposed porous ZIF-67 polyhedron with ultrahigh catalytic activity and stability on hydrogen generation, Renew. Energy 136 (2019) 1064–1070, https://doi.org/10.1016/j.renene.2018.09.070.

[18] F. Yang, J. Ruan, T. Li, Y. Zou, C. Xiang, F. Xu, L. Sun, Hydrolysis of sodium borohydride using a highly stable catalyst of ruthenium nanoparticles supported by cobalt–nickel hydroxide-coated nickel foam, J. Alloys Compd. 926 (2022) 166902, https://doi.org/10.1016/j.jallcom.2022.166902.

[19] Y. Li, G. Yang, L. Wei, J. Liu, Y. Zhang, Y. Cui, Y. Zhou, Magnetically recyclable Co_2P nanosheets as highly efficient catalysts for hydrogen generation from hydrolysis of sodium borohydride, New J. Chem. 46 (2022) 8256–8262, https://doi.org/10.1039/d2nj00966h.

[20] J. Meng, Z. Tong, H. Sun, Y. Liu, S. Zeng, J. Xu, Q. Xia, Q. Pan, S. Dou, H. Yu, Metal-free boron/phosphorus co-doped nanoporous carbon for highly efficient benzyl alcohol oxidation, Adv. Sci. 9 (2022) e2200518, https://doi.org/10.1002/advs.202200518.

[21] X. Yin, R. Cai, X. Dai, F. Nie, Y. Gan, Y. Ye, Z. Ren, Y. Liu, B. Wu, Y. Cao, X. Zhang, Electronic modulation and surface reconstruction of cactus-like CoB_2O_4@FeOOH heterojunctions for synergistically triggering oxygen evolution reactions, J. Mater. Chem. A 10 (2022) 11386–11393, https://doi.org/10.1039/d2ta01929a.

[22] Y. Li, X. Zhang, Q. Zhang, J. Zheng, N. Zhang, B. Chen, K. Smith, Activity and kinetics of ruthenium supported catalysts for sodium borohydride hydrolysis to hydrogen, RSC. Adv. 6 (2016) 29371–29377, https://doi.org/10.1039/c6ra00747c.

[23] J. Zhang, Y. Li, L. Yang, F. Zhang, R. Li, H. Dong, Ruthenium nanosheets decorated cobalt foam for controllable hydrogen production from sodium borohydride hydrolysis, Catal. Lett. 152 (2022) 1386–1391, https://doi.org/10.1007/s10562-021-03730-5.

[24] T. Avcı Hansu, Exergy and energy analysis of hydrogen production by the degradation of sodium borohydride in the presence of novel Ru based catalyst, Int. J. Hydrogen Energy 48 (2023) 6778–6787, https://doi.org/10.1016/j.ijhydene.2022.03.189.

[25] J. Jiang, S. Yang, H. Lei, L. Ai, Highly dispersed cobalt nanoparticles onto nitrogen-doped carbon nanosheets for efficient hydrogen generation via catalytic hydrolysis of sodium borohydride, Int. J. Hydrogen Energy 46 (2021) 32403–32412, https://doi.org/10.1016/j.ijhydene.2021.07.073.

[26] T. Avcı Hansu, A novel and active ruthenium based supported multiwalled carbon nanotube tungsten nanoalloy catalyst for sodium borohydride hydrolysis, Int. J. Hydrogen Energy 48 (2023) 6788–6797, https://doi.org/10.1016/j.ijhydene.2022.04.269.

[27] H. Li, Z. Liu, L. Wang, M. Guo, T.T. Isimjan, X. Yang, Bifunctional Ru-cluster-decorated Co_3B-$Co(OH)_2$ hybrid catalyst synergistically promotes $NaBH_4$ hydrolysis and water splitting, Chem. Eur. J. 29 (2023) e202203207, https://doi.org/10.1002/chem.202203207.

[28] L. Sun, Y. Meng, X. Kong, H. Ge, X. Chen, C. Ding, H. Yang, D. Li, X. Gao, J. Dou, Novel high dispersion and high stability cobalt-inlaid carbon sphere catalyst for hydrogen generation from the hydrolysis of sodium borohydride, Fuel 310 (2022) 122276, https://doi.org/10.1016/j.fuel.2021.122276.

[29] J. Chi, W. Gao, L. Zhang, B. Dong, K. Yan, J. Lin, B. Liu, Y. Chai, C. Liu, Induced phosphorization-derived well-dispersed molybdenum phosphide nanoparticles encapsulated in hollow N-Doped carbon nanospheres for efficient hydrogen evolution, ACS Sustain. Chem. Eng. 6 (2018) 7676–7686, https://doi.org/10.1021/acssuschemeng.8b00529.

[30] M. Guo, M. Xu, Y. Qu, C. Hu, P. Yan, T.T. Isimjan, X. Yang, Electronic/mass transport increased hollow porous Cu_3P/MoP nanospheres with strong electronic interaction for promoting oxygen reduction in Zn-air batteries, Appl. Catal. B Environ. 297 (2021) 120415, https://doi.org/10.1016/j.apcatb.2021.120415.

[31] M. Liu, K. Shi, Z. Duan, M. Zhang, Y. Xu, Z. Wang, X. Li, L. Wang, H. Wang, P-modified hollow carbon mesoporous nanospheres decorated with ultrafine OsP alloy nanoparticles for nonacidic hydrogen evolution, J. Mater. Chem. A 10 (2022) 13042–13047, https://doi.org/10.1039/d2ta02161g.

[32] S. Zhou, Y. Yang, W. Zhang, X. Rao, P. Yan, T.T. Isimjan, X. Yang, Structure-regulated Ru particles decorated P-vacancy-rich CoP as a highly active and durable catalyst for $NaBH_4$ hydrolysis, J. Colloid Interface Sci. 591 (2021) 221–228, https://doi.org/10.1016/j.jcis.2021.02.009.

[33] W. Zhang, Q. Li, C. Wang, J. Ma, C. Wang, H. Peng, Y. Wen, H. Fan, High sensitivity and selectivity chlorine gas sensors based on 3D open porous SnO_2 synthesized by solid-state method, Ceram. Int. 45 (2019) 20566–20574, https://doi.org/10.1016/j.ceramint.2019.07.036.

[34] X. Zhang, R. Zhao, Q. Wu, W. Li, C. Shen, L. Ni, H. Yan, G. Diao, M. Chen, Petal-like MoS_2 nanosheets space-confined in hollow mesoporous carbon spheres for enhanced lithium storage performance, ACS Nano 11 (2017) 8429–8436, https://doi.org/10.1021/acsnano.7b04078.

[35] F. Li, J. Xu, X. Yu, L. Chen, J. Zhou, Z. Yang, X. Xin, One-step solid-state reaction synthesis and gas sensing property of tin oxide nanoparticles, Sens. Actuators B Chem. 81 (2002) 165–169, https://doi.org/10.1016/s0925-4005(01)00947-9.

[36] J. Liu, G. Ning, K. Shi, M. Zheng, Y. Sun, Y. Gao, Y. Zhang, H. Wang, N-doped hollow porous carbon spheres@Co Cu Fe alloy nanospheres as novel non-precious metal electrocatalysts for HER and OER, Int. J. Hydrogen Energy 47 (2022) 5947–5960, https://doi.org/10.1016/j.ijhydene.2021.11.204.

[37] M. Farrag, Ultrasmall bimetallic Ru-Co alloy nanoclusters immobilized in amino-functionalized UiO-66 and N-doped carbonaceous zirconium oxide nanocomposite for hydrogen generation, J. Alloys Compd. 920 (2022) 165893, https://doi.org/10.1016/j.jallcom.2022.165893.

[38] Y. Yang, Y. Huang, S. Zhou, Y. Liu, L. Shi, T.T. Isimjan, X. Yang, Delicate surface vacancies engineering of Ru doped MOF-derived Ni-NiO@C hollow microsphere superstructure to achieve outstanding hydrogen oxidation performance, J. Energy Chem. 72 (2022) 395–404, https://doi.org/10.1016/j.jechem.2022.06.011.

[39] Y. Cao, Y. Su, L. Xu, X. Yang, Z. Han, R. Cao, G. Li, Oxygen vacancy-rich amorphous FeNi hydroxide nanoclusters as an efficient electrocatalyst for water oxidation,

J. Energy Chem. 71 (2022) 167–173, https://doi.org/10.1016/j.jechem.2022.03.044.
[40] B. Coşkuner Filiz, A. Kantürk Figen, S. Pişkin, The remarkable role of metal promoters on the catalytic activity of Co-Cu based nanoparticles for boosting hydrogen evolution: ammonia borane hydrolysis, Appl. Catal. B Environ. 238 (2018) 365–380, https://doi.org/10.1016/j.apcatb.2018.07.031.
[41] S. Joseph, D.M. Kempaiah, M. Benzigar, A.V. Baskar, S.N. Talapaneni, S.H. Jhung, D.H. Park, A. Vinu, Metal organic framework derived mesoporous carbon nitrides with a high specific surface area and chromium oxide nanoparticles for CO_2 and hydrogen adsorption, J. Mater. Chem. A 5 (2017) 21542–21549, https://doi.org/10.1039/c7ta06969c.
[42] J. Li, X. Hong, Y. Wang, Y. Luo, P. Huang, B. Li, K. Zhang, Y. Zou, L. Sun, F. Xu, F. Rosei, S.P. Verevkin, A.A. Pimerzin, Encapsulated cobalt nanoparticles as a recoverable catalyst for the hydrolysis of sodium borohydride, Energy Storage Mater. 27 (2020) 187–197, https://doi.org/10.1016/j.ensm.2020.01.011.
[43] H. Wang, Y. Wang, L. Tan, L. Fang, X. Yang, Z. Huang, J. Li, H. Zhang, Y. Wang, Component-controllable cobalt telluride nanoparticles encapsulated in nitrogen-doped carbon frameworks for efficient hydrogen evolution in alkaline conditions, Appl. Catal. b: Environ. (2018), https://doi.org/10.1016/j.apcatb.2018.11.081.
[44] Y. Huang, Z. Zhan, T. Lei, P. Yin, Amorphous CoFeB on nickel foam as a high efficient electrocatalyst for hydrogen evolution reaction, Int. J. Hydrogen Energy 47 (2022) 12539–12546, https://doi.org/10.1016/j.ijhydene.2022.01.247.
[45] H.S. Gujral, G. Singh, J.H. Yang, C.I. Sathish, J.B. Yi, A. Karakoti, M. Fawaz, K. Ramadass, A.H. Al-Muhtaseb, X.J. Yu, M.B.H. Breese, A. Vinu, Mesoporous titanium carbonitride derived from mesoporous C_3N_5 for highly efficient hydrogen evolution reaction, Carbon 195 (2022) 9–18, https://doi.org/10.1016/j.carbon.2022.03.060.
[46] A.D. Molchanova, M.A. Prosnikov, V.P. Petrov, R.M. Dubrovin, S.G. Nefedov, D. Chernyshov, A.N. Smirnov, V.Y. Davydov, K.N. Boldyrev, V.A. Chernyshev, R. V. Pisarev, M.N. Popova, Lattice dynamics of cobalt orthoborate $Co_3(BO_3)_2$ with kotoite structure, J. Alloys Compd. 865 (2021) 158797, https://doi.org/10.1016/j.jallcom.2021.158797.
[47] D. Guerniche, C. Ait Ramdane-Terbouche, A. Terbouche, M. Khalfaoui, C.-L. Douib, H. Belkhalfa, R. Boukherroub, A. Benchettara, Novel hybrid material based on Ru complex and its RuO_2 oxide for dopamine and dopamine-uric acid simultaneous determination, J. Organomet. Chem. 997 (2023) 122769, https://doi.org/10.1016/j.jorganchem.2023.122769.
[48] M. Mariyappan, S. Arunkumar, K. Marimuthu, Concentration effect on the structural and spectroscopic investigations of Sm^{3+} ions doped B_2O_3–Bi_2O_3–CaF_2–Na_2O glasses, J. Lumin. 196 (2018) 151–160, https://doi.org/10.1016/j.jlumin.2017.12.026.
[49] B. Barman, B. Sarkar, K. Nanda, Pd-coated Ru nanocrystals supported on N-doped graphene as HER and ORR electrocatalysts, Chem. Commun. 55 (2019) 13928–13931, https://doi.org/10.1039/c9cc06208d.
[50] M. Guo, Z. Huang, Y. Qu, L. Wang, H. Li, T.T. Isimjan, X. Yang, Synergistic effect and nanostructure engineering of three-dimensionally hollow mesoporous spherical Cu_3P/TiO_2 in aqueous/flexible Zn–air batteries, Appl. Catal. B Environ. 320 (2023) 121991, https://doi.org/10.1016/j.apcatb.2022.121991.
[51] S. Zhou, H. Jang, Q. Qin, L. Hou, M.G. Kim, S. Liu, X. Liu, J. Cho, Boosting hydrogen evolution reaction by phase engineering and phosphorus doping on Ru/P-TiO_2, Angew. Chem. Int. Ed. 61 (2022) e202212196, https://doi.org/10.1002/anie.20221219.
[52] K. Wang, S. Wang, K. Hui, H. Gao, D. Dinh, C. Yuan, C. Zha, Z. Shao, Z. Tang, K. Hui, Synergistically boosting the elementary reactions over multiheterogeneous ordered macroporous Mo_2C/NC-Ru for highly efficient alkaline hydrogen evolution, Carbon, Energy 4 (2022) 856–866, https://doi.org/10.1002/cey2.188.
[53] F. Li, J. Li, L. Chen, Y. Dong, P. Xie, Q. Li, Hydrogen production through hydrolysis of sodium borohydride: highly dispersed CoB particles immobilized in carbon nanofibers as a novel catalyst, Int. J. Hydrogen Energy 45 (2020) 32145–32156, https://doi.org/10.1016/j.ijhydene.2020.08.137.
[54] Y. Meng, Q. Sun, T. Zhang, J. Zhang, Z. Dong, Y. Ma, Z. Wu, H. Wang, X. Bao, Q. Sun, J. Yu, Cobalt-promoted noble-metal catalysts for efficient hydrogen generation from ammonia borane hydrolysis, J. Am. Chem. Soc. 145 (2023) 5486–5495, https://doi.org/10.1021/jacs.3c00047.
[55] B. Cui, G. Wu, S. Qiu, Y. Zou, E. Yan, F. Xu, L. Sun, H. Chu, Ruthenium supported on cobalt-embedded porous carbon with hollow structure as efficient catalysts toward ammonia-borane hydrolysis for hydrogen production, Adv. Sust. Syst. 5 (2021) 2100209, https://doi.org/10.1002/adsu.202100209.
[56] Q. Wei, S. Qiu, C. Yin, J. Liu, Y. Xia, X. Wen, Y. Zou, F. Xu, L. Sun, H. Chu, Nitrogen-doped carbon encapsulated Ru-decorated Co_2P supported on graphene oxide as efficient catalysts for hydrogen generation from ammonia borane, J. Alloys Compd. 921 (2022) 166207, https://doi.org/10.1016/j.jallcom.2022.166207.
[57] H. Xue, A. Meng, T. Yang, Z. Li, C. Chen, Controllable oxygen vacancies and morphology engineering: Ultra-high HER/OER activity under base–acid conditions and outstanding antibacterial properties, J. Energy Chem. 71 (2022) 639–651, https://doi.org/10.1016/j.jechem.2022.04.052.
[58] G.M. Arzac, M. Paladini, V. Godinho, A.M. Beltran, M.C. Jimenez de Haro, A. Fernandez, Strong activation effect on a Ru-Co-C thin film catalyst for the hydrolysis of sodium borohydride, Sci. Rep. 8 (2018) 9755, https://doi.org/10.1038/s41598-018-28032-6.
[59] A.D. Chowdhury, N. Agnihotri, A. De, Hydrolysis of sodium borohydride using Ru–Co-PEDOT nanocomposites as catalyst, Chem. Eng. J. 264 (2015) 531–537, https://doi.org/10.1016/j.cej.2014.11.108.
[60] S. Zhou, L. Cheng, Y. Huang, Y. Liu, L. Shi, T.T. Isimjan, X. Yang, Constructing Ru particles decorated Co_3B-CoP heterostructures as a highly active and reusable catalyst for H_2 generation by catalyzing $NaBH_4$ hydrolysis, Appl. Catal. b: Environ. 328 (2023) 122519, https://doi.org/10.1016/j.apcatb.2023.122519.
[61] L. Shi, K. Zhu, Y. Yang, Y. Liu, S. Xu, T.T. Isimjan, X. Yang, Oxygen-vacancy-rich Ru-clusters decorated Co/Ce oxides modifying ZIF-67 nanocubes as a high-efficient catalyst for $NaBH_4$ hydrolysis, Int. J. Hydrogen Energy 47 (2022) 37840–37849, https://doi.org/10.1016/j.ijhydene.2022.08.289.
[62] U.B. Demirci, P. Miele, Reaction mechanisms of the hydrolysis of sodium borohydride: a discussion focusing on cobalt-based catalysts, C. r. Chim. 17 (2014) 707–716, https://doi.org/10.1016/j.crci.2014.01.012.
[63] J. Andrieux, U.B. Demirci, P. Miele, Langmuir-Hinshelwood kinetic model to capture the cobalt nanoparticles-catalyzed hydrolysis of sodium borohydride over a wide temperature range, Catal. Today 170 (2011) 13–19, https://doi.org/10.1016/j.cattod.2011.01.019.
[64] C.Z.G. Guella, B. Patton, A. Miotello, New insights on the mechanism of palladium-catalyzed hydrolysis of sodium borohydride from ^{11}B NMR measurements, J. Phys. Chem. B 110 (2006) 17024–17033, https://doi.org/10.1021/jp063362n.